Meandering ocean currents modulate mid-latitude storm energetics

Félix Vivant[1] **and Guillaume Lapeyre**[1]

[1]LMD-IPSL, ENS, PSL Université, Ecole Polytechnique, IP Paris, Sorbonne Université, CNRS, Paris, France

Key Points:

- Idealized simulations are used to examine how atmospheric cyclogenesis responds to meanders of large-scale ocean currents
- Moisture supply above the warm side of the meander triggers diabatic heating a few hours after each crossing of the ocean front
- Cyclone intensification is modulated by ocean meandering fronts and depends on the scale of the meanders

Corresponding author: Félix Vivant, `felix.vivant@lmd.ipsl.fr`

Abstract

Extratropical cyclones primarily develop over the western parts of ocean basins, where strong sea surface temperature (SST) fronts form along western boundary currents. The influence on cyclogenesis of these SST fronts, whose paths often meander on scales of hundreds of kilometers, remains incompletely understood. Here, we use idealized simulations to examine the sensitivity of storm development to SST meanders of varying size. Large-scale meanders (1000 km) cause earlier intensification and decay compared to smaller-scale meanders (500 km) or a zonal SST front. Each crossing from the cold to the warm sides of the meanders locally enhances moisture supply into the atmospheric boundary layer, triggering peaks in diabatic heating within the free-troposphere a few hours later. This, in turn, amplifies eddy kinetic energy in both surface and upper-level anomalies within hours. These results emphasize the interplay between the trajectory of storms and the ocean meanders on cyclone life cycles.

Plain Language Summary

Mid-latitude storms are large weather systems, about 1000 km across, that last a few days and strongly influence weather at mid-latitudes. These storms often develop over the western parts of ocean basins, above major ocean currents such as the Gulf Stream in the Atlantic or the Kuroshio in the Pacific. These ocean currents are known to intensify storm by supplying moisture to the atmosphere through surface evaporation, which contributes to cloud formation and precipitation. One of their specificity is that they often form meanders with high sea surface temperature contrasts, which may affect the atmospheric cyclone life cycle. Using a weather forecast model in an idealized setting, we show that when a cyclone passes over the warm side of the meanders, moisture and precipitation locally increase, strengthening storms within hours. These meanders also shift the timing of storm intensification by tens of hours, highlighting the rapid response of storms to ocean temperature contrasts.

1 Introduction

Mid-latitude storms tend to form over western boundary currents (WBCs) such as the Kuroshio-Oyashio Extension—regions characterized by strong meridional sea surface temperature (SST) gradients extending over thousands of kilometers (Shaw et al., 2016). These SST fronts help maintain strong low-level baroclinicity, i.e., strong horizontal temperature gradients of the mean atmospheric flow, through surface sensible heat fluxes (SHF), thereby anchoring storm tracks (Nakamura et al., 2004; Brayshaw et al., 2008; Derem-

ble et al., 2012). In addition, WBCs act as major sources of atmospheric moisture via surface latent heat flux (LHF), which modulates diabatic heating associated to cloud formation and precipitation within storms (Hirata et al., 2015; Sheldon et al., 2017; Demirdjian et al., 2022). As a result, SST fronts contribute to the intensification of extratropical cyclones over several days through both baroclinic and diabatic pathways, acting as key sources of eddy kinetic energy (Lorenz, 1955). Integrated over time, storm-WBCs interaction is noticeable in climatological data, with convective activity and precipitation patterns consistently localized above SST fronts (Minobe et al., 2008; Vannière et al., 2017; Larson et al., 2024), emphasizing the major role of WBCs in driving weather and climate at mid-latitudes.

Several studies have investigated the sensitivity of individual storm events to the characteristics of the underlying SST front. A uniform increase in absolute SST by 1°C has been shown to further deepen surface cyclones by several hPa, primarily due to enhanced diabatic heating (Booth et al., 2012; Bui & Spengler, 2021). Likewise, shifting the SST distribution poleward or increasing its meridional gradient modifies the SST encountered during cyclogenesis, promoting more explosive storm development (de Vries et al., 2019; Bui & Spengler, 2021) and changes in atmospheric frontal frequency (Parfitt et al., 2016). Thus far, most sensitivity experiments of this kind have focused on zonally-symmetric characteristics of SST fronts. However, WBCs and their extensions are actually not zonally symmetric; they can form meanders with typical scales of a few hundreds km, which can persist for a year or evolve over weeks (Kelly et al., 2010; Qiu et al., 2014). Notably, the large cold meander of the Kuroshio Extension has been shown to reduce surface LHF, inhibit storm intensification, and shift cyclone tracks southward (Nakamura et al., 2012; Hayasaki et al., 2013). Ocean meanders—and more generally, mesoscale SST anomalies (with horizontal scales of ∼200 km)—modulate mid-latitude diabatic heating, thereby influencing both synoptic-scale cyclogenesis (Joyce et al., 2009; Zhang et al., 2019) and the mean atmospheric circulation (O'Reilly & Czaja, 2015; Ma et al., 2017; Foussard et al., 2019).

In this regards, understanding the pathways and timescales through which SST anomalies modulate cyclone intensification is of interest, especially for meandering SST fronts that better represent WBCs than zonal fronts. Here, we use idealized simulations to investigate the sensitivity of cyclone life cycles to SST meanders of varying size. Storm energetics are analyzed through an eddy available potential energy (EAPE) budget following Lorenz (1955), with a particular focus on diabatic processes.

2 Methods and experiment design

2.1 Model and initial conditions

Simulations are performed with the Weather Research and Forecast (WRF) regional model version 4.3.3 (Skamarock et al., 2019), with physical parameterizations for surface fluxes (Jiménez et al., 2012), planetary boundary layer (PBL) turbulence (Mellor & Yamada, 1982), microphysics (Chen & Sun, 2002) and cumulus (Kain, 2004). No radiative model is used and the atmosphere is forced by the ocean through SST. Experiments are conducted on the f-plane (45 °N) in a zonally periodic channel, of size 16000 km by 6000 km in the zonal (x) and meridional (y) directions, respectively. In the vertical, the domain extends from the surface to a height of 25 km. Simulations are run over a 5-day period with a horizontal resolution of 20 km and with 61 vertical layers stretched close to the surface (15 layers below 1 km).

The initial atmospheric state is adapted from Bui and Spengler (2021) and consists of a zonally symmetric jet and a cyclonic perturbation, identical across all experiments. The zonal wind speed of the baroclinic jet is about 5 m s^{-1} at the surface and reaches 50 m s^{-1} at the tropopause ($\sim$ 8 km height). The cyclonic anomaly radius is 500 km and corresponds to a maximum wind anomaly of 5 m s^{-1} at the surface (Figure 1). A detailed description of the experiment design is given in Supporting Information S1.

In the control (CTL) experiment, the SST distribution is fixed in time and corresponds to a large-scale, zonally symmetric ocean front, with a maximum SST gradient of 3 °C per 100 km centered at $y = 0$ (Figure 1a). To investigate the role of SST geometry, we introduce sinusoidal SST fronts extending 4000 km zonally in two additional experiments, M5 and M10, with characteristic wavelengths of 500 km and 1000 km, respectively (Figure 1b, c). The meanders are located 1000 km downstream (east) of the initial cyclonic perturbation, allowing time for the atmosphere to spin up before the cyclone interacts with the ocean meanders (Figure 1). The maximum meridional SST gradient in M5 and M10 is identical to that in CTL (3 °C per 100 km), ensuring that differences in the cyclones life cycle should come from differences in the geometry of the SST front.

2.2 Diagnostics and energy budget

The evolution of cyclone intensity is analyzed using both sea level pressure (SLP) diagnostics and an energy budget along its trajectory. Here, the cyclone center is defined as the location of the minimum in SLP zonal anomaly (Figure 1), while surface intensity is the sea level pressure at the cyclone center, denoted SLP_c herein. We define the maximum intensification as the time of the most rapid SLP_c decrease, and the maximum in-

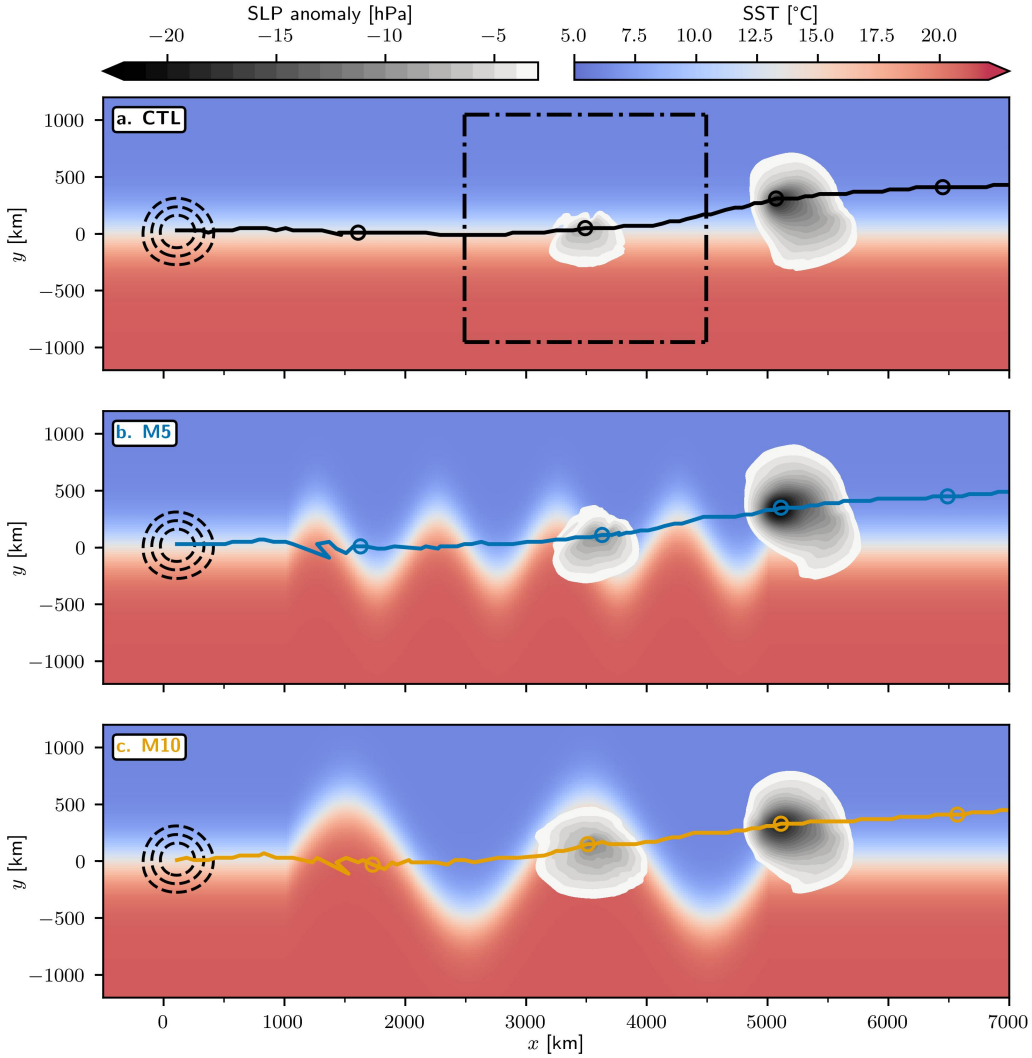

Figure 1. Storm development over ocean meanders of varying size. (a) CTL, (b) M5 and (c) M10 experiments. Initial cyclonic perturbation, 1 h after the start of the simulations, represented by black dashed sea level pressure anomaly contours (-1.5, -1, and -0.5 hPa). Storm trajectory (solid line) marked every 24 hours with circles, sea level pressure anomaly at 48 h and 72 h (gray shading) and sea surface temperature (color shading). (a) The dash-dotted square represents the cyclone domain at 48 h for CTL.

tensity as the time of minimum SLP_c. Additionally, we examine the eddy available potential energy (EAPE) budget associated with the cyclone (Lorenz, 1955; Moore & Montgomery, 2005; Bui & Spengler, 2021). This budget is computed from spatial averages over a 2000 km $\times$2000 km domain centered on the cyclone (referred to as the cyclone domain herein) and vertically averaged over the troposphere (from 950 hPa to 100 hPa). It is written as:

$$\frac{\partial}{\partial t}A_E = C_A + G_E - C_E + R_{A_E} \tag{1}$$

where A_E is EAPE, C_A the baroclinic production, G_E the diabatic production and C_E the conversion from A_E to eddy kinetic energy (EKE). R_{A_E} is a residual term coming from numerical approximations, dissipation, and lateral fluxes through the open boundaries of the cyclone domain. Here, we focus on the following terms:

$$A_E = \Big\{ g\frac{T^{*2}}{2\overline{\sigma}} \Big\}_{\mathrm{cyc}} \tag{2}$$

$$K_E = \Big\{ \frac{u^{*2}+v^{*2}}{2} \Big\}_{\mathrm{cyc}} = \Big\{ k_e \Big\}_{\mathrm{cyc}} \tag{3}$$

$$C_E = \Big\{ -R_d\frac{T^*\omega^*}{p} \Big\}_{\mathrm{cyc}} \tag{4}$$

$$G_E = \Big\{ g\frac{T^*}{\overline{\sigma}}\frac{Q^*}{c_p} \Big\}_{\mathrm{cyc}} = \Big\{ g_e \Big\}_{\mathrm{cyc}} \tag{5}$$

$$C_A = \Big\{ -g\frac{T^*}{\overline{\sigma}}\Big(v^*\frac{\partial}{\partial y} + \omega^*\frac{\partial}{\partial p}\Big)[T]' \Big\}_{\mathrm{cyc}} \tag{6}$$

where

$$\overline{\sigma} = g\Big(\frac{\overline{T}}{c_p} - \frac{p}{R_d}\frac{\partial \overline{T}}{\partial p} \Big) \tag{7}$$

is the horizontally averaged static stability and K_E is EKE. The diabatic heating Q is the sum of the heating associated with the microphysics, cumulus, and PBL parameterizations. For any variable X, $[X]$ is its zonal average and $\overline{X}$ denotes its horizontal mean over the entire domain, while $\overline{X}^{\mathrm{cyc}}$ stands for the horizontal mean over the cyclone domain only. With these notations, $X^* = X - [X]$ is the zonal anomaly, while $X' = X -$

$\overline{X}$ is the horizontal anomaly. We also introduce the quantity $\{X\}_{\text{cyc}}$ which is both vertically integrated and horizontally averaged over the cyclone domain:

$$\left\{X\right\}_{\text{cyc}} = \frac{1}{g} \int_{100\,\text{hPa}}^{950\,\text{hPa}} \overline{X}^{\text{cyc}}\, dp \tag{8}$$

Finally, we note $\widetilde{X} = \int_{100\ \text{hPa}}^{950\ \text{hPa}} X dp/g$. To ensure the accuracy of the EAPE budget (Equation 1), we verified that the residual term remains five times smaller in absolute value than the other terms when the budget is computed over the entire domain, i.e., using $\overline{X}$ instead of $\overline{X}^{\text{cyc}}$ in (8). When restricting the budget to the cyclone domain, R_{A_E} was found to be always negative and twice smaller than the other terms during the first 60 hours. At later times, it increases in magnitude which may be due to lateral fluxes radiating energy outward from the open cyclone domain to the surrounding environment. We expect it should not affect the interpretation of the EAPE budget, especially during the early stages of development.

3 Results

3.1 Time evolution of cyclone energetics

Surface cyclones in the CTL, M5, and M10 experiments have similar trajectories, traveling approximately 5000 km eastward during the first 72 h due to jet stream advection and about 500 km northward (Figure 1). In M5 and M10, the cyclones develop over ocean meanders for approximately two days, from 20 h to 70 h (Figure 1b, c). In all three experiments, the sea level pressure at the cyclone center, SLP_c, decreases during the first 70 h (deepening phase), and then increases during the decaying phase (Figure 2a). Notable differences emerge in the timing of maximum intensification (i.e., SLP_c drop), occurring at 48 h in M10, 60 h in M5, and 68 h in CTL (Figure 2a). The maximum intensity also varies across the experiments, with the most intense surface cyclone reaching 976 hPa in M5, 2 hPa and 3 hPa deeper compared to CTL and M10, respectively (Figure 2a). These differences are also reflected in the full SLP field, with earlier development in M10 at 48 h and a deeper storm in M5 at 72 h (Figure 1). Regarding K_E (Figure 2a), its temporal evolution aligns with that of SLP_c, showing similar differences between experiments in terms of intensification, but with a maximum in K_E reached a few hours after the SLP_c minimum. A notable exception arises after 90 h, when K_E in CTL exceeds that in M5, despite M5 having a lower SLP_c (Figure 2a). This is because K_E accounts for both surface and tropopause anomalies, while SLP_c reflects only surface in-

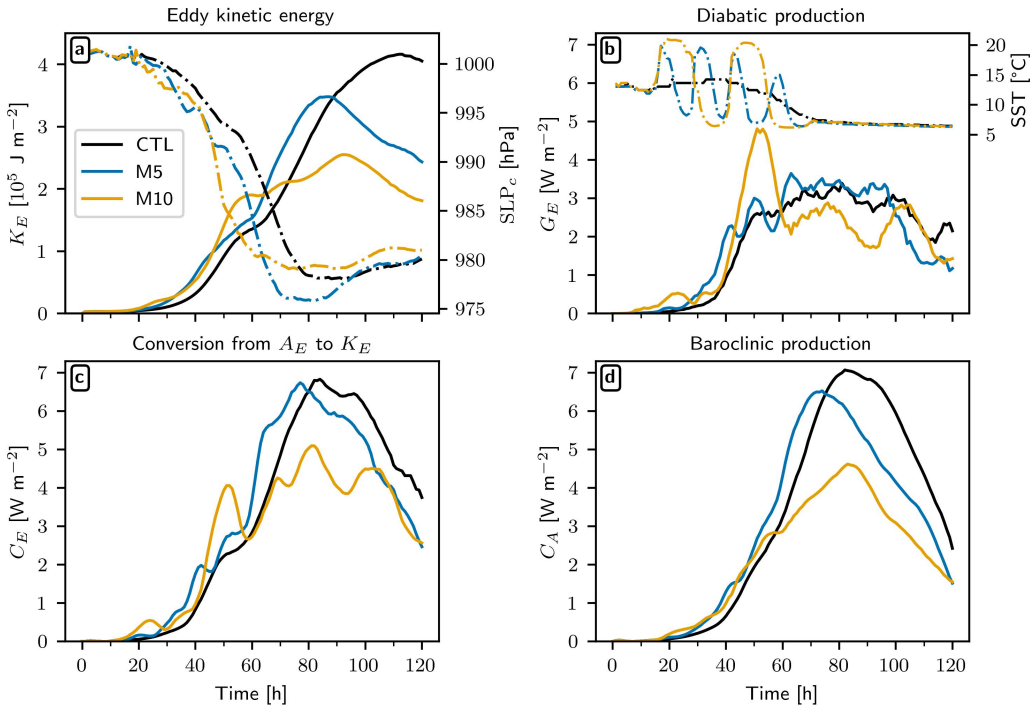

Figure 2. Storm energetic response to ocean meanders. (a) Eddy kinetic energy (K_E, solid lines) and sea level pressure at the cyclone center (SLP$_c$, dash-dotted lines). (b) Diabatic production (G_E, solid lines) of eddy available potential energy (A_E) and sea surface temperature underneath the cyclone center (dash-dotted lines). (c) Conversion from A_E to K_E (C_E, solid lines). (d) Baroclinic production of A_E (C_A, solid lines). K_E, G_E, C_E and C_A are vertically integrated and horizontally averaged quantities over the cyclone domain (see Methods). Black, blue and orange lines correspond to CTL, M5 and M10 experiments, respectively.

tensity. These differences in intensity across the experiments can be traced back to the presence of ocean meanders, which are the sole differences between the experiments.

The modulation of cyclone intensity by the SST meanders mainly results from the modulation of sensible and latent heat energy exchanges at the ocean surface which later modifies the atmospheric temperature and subsequently the EAPE budget. In particular, the conversion term from A_E to K_E, C_E, is found to be greater in M10 than in M5 and CTL during the first 60 h, in agreement with the differences observed in K_E increase (Figure 2a, c). Afterwards, while the conversion term C_E remains positive for M10, K_E does not change much, presumably due to barotropic effects (surface friction or exchanges with the mean flow) and ageostrophic geopotential fluxes (Orlanski & Sheldon, 1995). Two terms govern the increase in EAPE: the baroclinic production C_A, which is the extrac-

tion of potential energy from the mean flow and the diabatic production G_E, which is related to water condensation (Figure 2b, d).

The overall evolution of the conversion to EKE, C_E, is similar to that of C_A, with an increasing phase during the first 80 h, followed by a decreasing phase in all three experiments (Figure 2c, d). Additionally, G_E has a sharp increase around 30 h and in general exceeds C_A in amplitude up to 60 h, especially in M10. Note also that G_E has pronounced peaks in M5 and M10 that are also observed in C_E, but not in C_A (Figure 2b-d). These observations confirm that both baroclinic and diabatic productions contribute to C_E and are sources of K_E. However, during the deepening phase, the main source of differences between experiments comes from diabatic processes. In the following, we focus primarily on these processes.

3.2 Modulation of diabatic heating by ocean meanders

The peaks in G_E observed at 22 h and 52 h in M10, and at 41 h, 50 h, and 62 h in M5 (Figure 2b) are related to the ocean meanders. These local maxima occur a few hours after the cyclone center passes over the warm side of the ocean meanders, as shown by the corresponding variation of G_E and the underlying SST in Figure 2b. For example, in experiment M10, the maximum value of G_E is attained at 52 h, after the cyclone passed over the warm side of the second meander at 47 h. Its value is 5 W m^{-2}, which is 2.1 W m^{-2} larger than in CTL. Simultaneously, C_E reaches 4 W m^{-2}, leading to a deep intensification, with K_E increased by 35% and SLP_c decreased by 10 hPa at 55 h compared to CTL (Figure 2a). As a result, the maximum intensification in M10 occurs 20 hours earlier than CTL (Figure 2a).

The influence of ocean meanders on the diabatic production is presented in Figure 3 for CTL and M10. The thick purple contour in Figure 3 delineates the warm sector—e.g., at $(x, y) = (3250\ \mathrm{km}, 0\ \mathrm{km})$ in Figure 3a—from the cold sector of the storms—e.g., at $(x, y) = (2500\ \mathrm{km}, -250\ \mathrm{km})$ in Figure 3a. The warm conveyor belt (WCB) above the warm sector carries upward and northward warm and humid air masses, while the dry intrusion above the cold sector carries downward and southward cold and dry air masses (Browning, 1997; Dacre et al., 2019). At 42 h, the warm sector of the cyclone of the M10 experiment is located above the warm side of the ocean meander, producing high surface latent heat fluxes (LHF) of up to 250 W m^{-2} (Figure 3c). In contrast, at the same instant, LHF reaches only 200 W m^{-2} in CTL, but located 1000 km upstream and in the cold sector (Figure 3a). The enhanced LHF in M10 increases the moisture supply in the warm sector of the cyclone, intensifying the northwestward moisture transport relative to its motion (see vectors in Figure 3c, d). Consequently, more moisture ascends

within the WCB in M10 than in CTL with vertical water vapor fluxes exceeding 1.5 kg m^{-2} s^{-1} at 750 hPa ($\sim$ 3 km height) compared to 1.25 kg m^{-2} s^{-1} in CTL (Figure 4a, c). The corresponding diabatic production strongly increases in the core of the cyclone (Figure 3d) at about 550 hPa (Figure 4c), which contributes to a stronger surface cyclone with surface pressure globally 5 hPa lower in M10 compared to CTL (Figure 3b, d). The delay between the time the cyclone is centered over the warm side of a meander (e.g., at 47 h in Figure 4c for M10) and the subsequent peak in diabatic production (e.g., at 52 h in Figure 4c) is about 5 to 10 h, which likely corresponds to the ascent time for surface air parcels to reach 5 km within the WCB (Bui & Spengler, 2021; Demirdjian et al., 2022). Diabatic production induced by ocean meanders affects not only the EKE of the surface cyclone (below the 600 hPa level) but also that of the upper-level anomalies (around 400 hPa, Figure 4b–c). For example, a distinct EKE response to a warm meander is seen at upper levels in M10, where $\overline{k_e}^{\text{cyc}}$ at 400 hPa increases from 15 J kg^{-1} at 42 h to 60 J kg^{-1} at 52 h (Figure 4c). These results show that the response to ocean meanders extends to the upper troposphere as well.

The local maxima of G_E in M5 are weaker than those in M10, although three different peaks are clearly associated with the SST meanders (Figures 2b and 4b, c). Specifically, a few hours after the cyclone passes over the warm side of the different meanders, additional moisture is transported within the WCB giving rise to three distinct maxima (Figure 4b). As the diabatic production in M5 is of the same order of magnitude as the baroclinic production, the effects of the meanders are less apparent in the C_E conversion term (Figure 2c). However, a greater K_E and a lower SLP$_c$ are reached in M5 than in M10 (Figure 2a).

3.3 Later stages of development

After 55 h, the M10 cyclone passes over the cold side of the meander (Figure 4d), which is 4 °C cooler than the SST in the other experiments. As a result, the vertical moisture transport decreases at 60 h (Figure 4c), consistent with a drop in diabatic production (Figures 2b and 4c) and C_E (Figure 2c). The resulting K_E is smaller, and SLP$_c$ higher, than those of M5 and CTL (Figure 2a). Note also that the baroclinic production term increases more slowly after 60 h for M10. To better understand this behavior, we analyse the expression of C_A (Equation 6), given that the vertical term can be neglected and that $\dfrac{\partial [T]'}{\partial y} = \dfrac{\partial [T]}{\partial y}$:

$$C_A \approx \left\{ T^* v^* \sqrt{\frac{g}{\overline{\sigma}}} \sigma_E \right\}_{\text{cyc}} \tag{9}$$

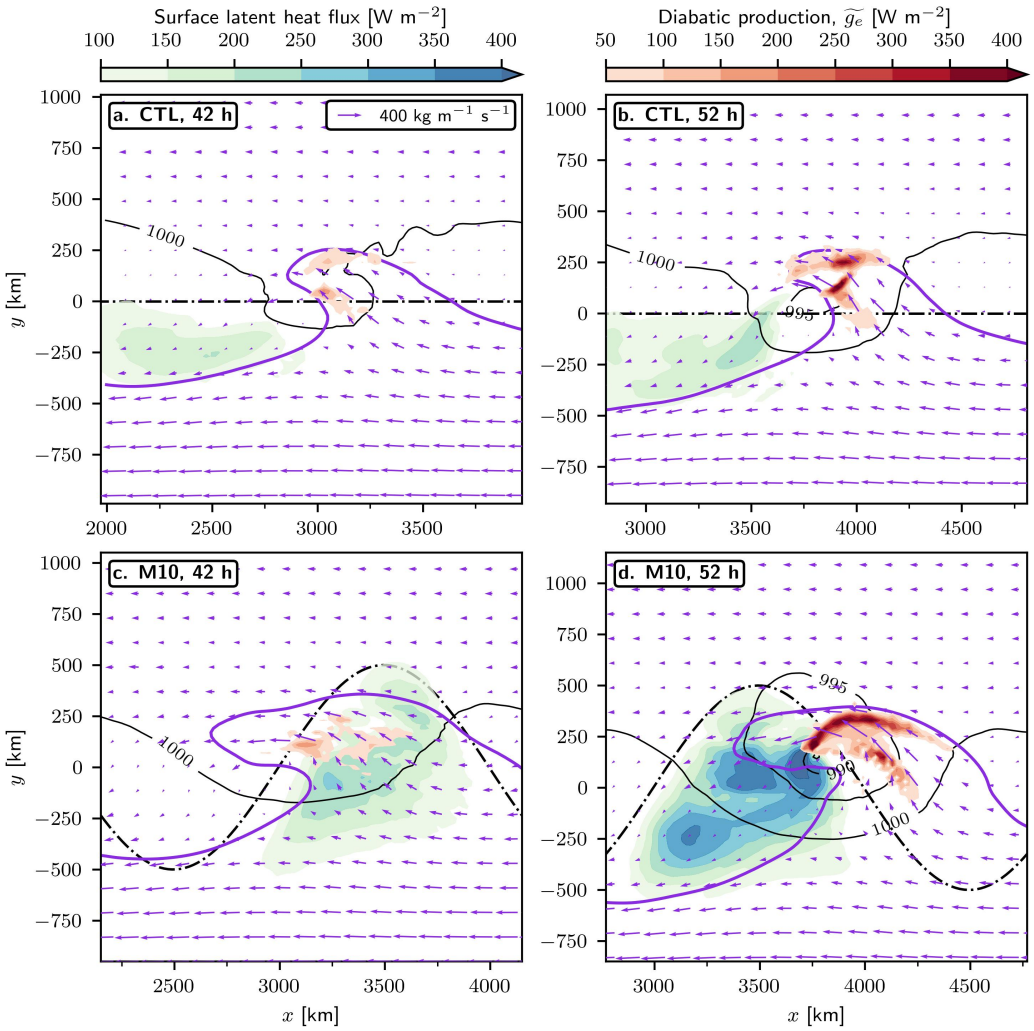

Figure 3. Moisture supply and diabatic production over a warm meander. (a, b) CTL and (c, d) M10 at (a, c) 42 h and (b, d) 52 h. Panels are centered on the cyclone center. Surface latent heat flux (blue-green shading), vertically integrated diabatic production (G_E, red shading), sea level pressure (solid black contours, in hPa) and vertically integrated horizontal moisture flux relative to the cyclone (purple arrows). The sea surface temperature front is denoted by a black dash-dotted line. The thick purple contour represents a vertically integrated water vapor content of 14 kg m^{-2}, delineating the warm sector (southeast) and the cold sector (northwest).

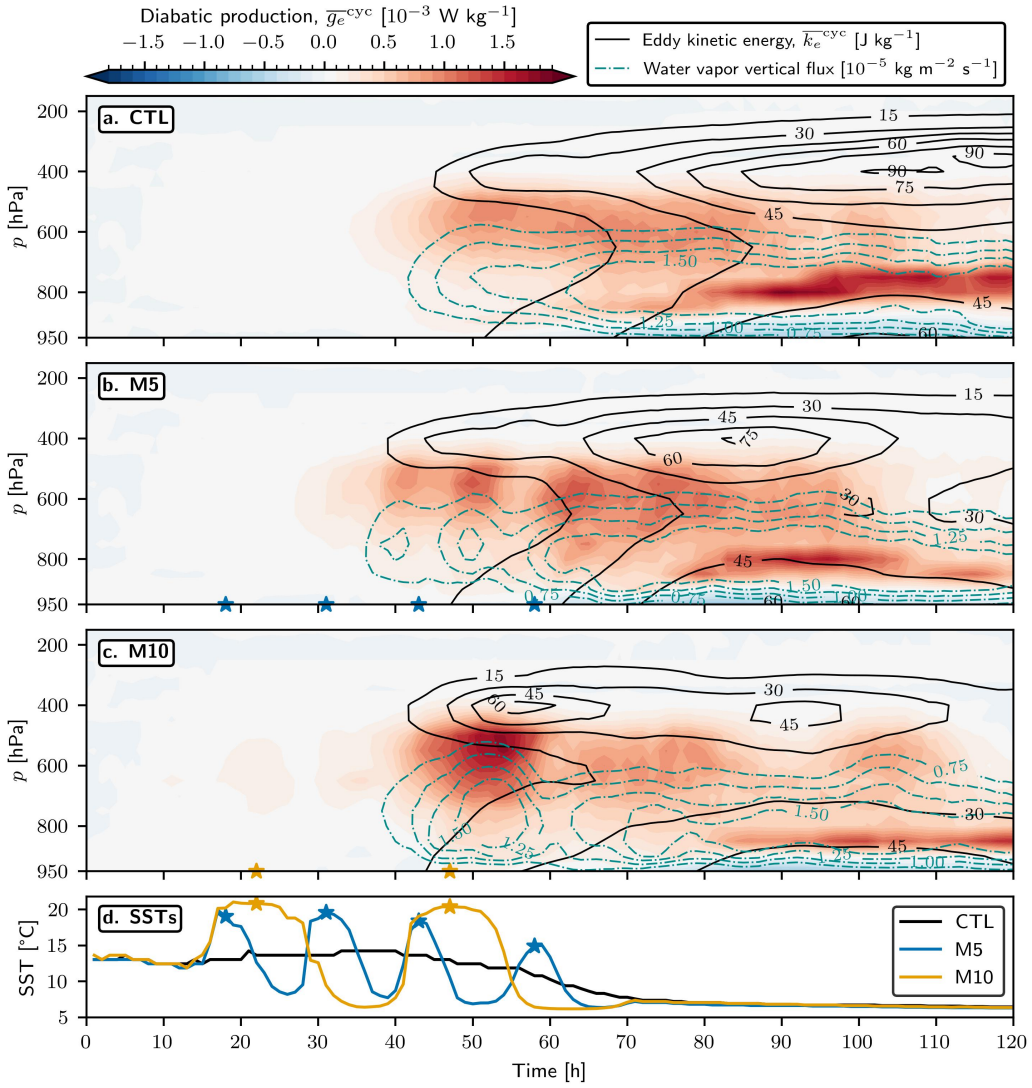

Figure 4. Hovmöller diagram and deep tropospheric response. (a–c) Diabatic production ($\overline{g_e}^{cyc}$, shading), eddy kinetic energy ($\overline{k_e}^{cyc}$, black contours), and vertical flux of water vapor averaged over the cyclone domain (cyan dash-dotted contours). Panels (a) CTL, (b) M5 and (c) M10 experiments. (d) Sea surface temperature underneath the cyclone center for CTL (black), M5 (blue), and M10 (orange). In (b–d), stars indicate times when the cyclone center is located above warm meanders.

where $T^*v^*\sqrt{g/\overline{\sigma}}$ is the meridional eddy heat flux and σ_E is the baroclinicity of the mean flow:

$$\sigma_E = -\sqrt{\frac{g}{\overline{\sigma}}}\frac{\partial[T]}{\partial y} \tag{10}$$

For each experiment, we compute the Eady growth rate as $0.31\,\overline{\sigma_E}^{\mathrm{cyc}}$ at 850 hPa, i.e., the low-level baroclinicity averaged over the cyclone domain. It remains relatively constant in time and across experiments, with a value around 0.65 day^{-1} (not shown). The evolution of C_A is indeed largely driven by eddy heat flux, with a Pearson correlation coefficient greater than 0.95 between C_A and $\{T^*v^*\sqrt{g/\overline{\sigma}}\}_{\mathrm{cyc}}$. A possible explanation for the weak growth of C_A in M10 after 55 h is that the cold and warm sectors of the cyclone are out of phase with respect to the warm and cold sides of the ocean meanders (Figure 3d). Because the atmospheric cold sector in M10 is above the ocean warm meander at 52 h, it is warmed by high fluxes reaching 400 W m^{-2} (Figure 3d), while the warm sector is cooled, thereby reducing the eddy heat flux (T^*v^*) and C_A afterwards (Figure 2d). A negative feedback might also be at play: a reduced K_E, i.e., a reduced v^*, extracts less energy from the mean flow (lower C_A), leading to a smaller K_E. Similarly in M5, G_E and C_A increase until the cyclone passes over the last warm meander ($\sim$ 70 h, Figure 2b, d), but this occurs later than in M10, explaining why higher K_E and lower SLP$_c$ are reached at later times (Figure 2a).

While the surface cyclone in M5 is the deepest among the three experiments, the largest K_E maximum is observed in CTL after 90 h (Figure 2a). This is consistent with the fact that C_A in CTL continues to increase the longest and attains the highest value. The elevated K_E actually corresponds to strong upper-level anomalies, with $\overline{k_e}^{\mathrm{cyc}}$ reaching 90 J kg^{-1} at 400 hPa compared to 45 J kg^{-1} in M5 (Figure 4a, b). In contrast, both experiments exhibit similar values of $\overline{k_e}^{\mathrm{cyc}}$ below 800 hPa ($\sim$ 50 J kg^{-1}, Figure 4a, b), in agreement with similar SLP$_c$ values after 90 h (Figure 2a).

4 Conclusions and discussion

In this study, we analyzed how meandering SST fronts modulate the energetics of a mid-latitude storm. Each time when the cyclone passes over the warm side of the ocean meander, surface latent heat fluxes strongly increase, leading to enhanced moisture supply in the atmospheric boundary layer. This triggers peaks in diabatic heating during the cyclone deepening phase, which in turn amplify EKE in both surface and upper-level anomalies within hours. This diabatic response leads to intensity differences of several hPa and shifts the maximum intensification by tens of hours. Large-scale meanders ($\sim$1000 km) lead to earlier storm intensification and decay, whereas smaller-scale meanders ($\sim$500 km)

sustain elevated baroclinic and diabatic production, yielding a deeper surface cyclone overall. When the cold and warm sectors of storms are out of phase with ocean meanders, baroclinic production is reduced, weakening upper-level anomalies relative to a zonal SST front—especially during the later stages of development. This finding aligns with previous work showing that the cold meander of the Kuroshio Extension inhibits storm intensification (Nakamura et al., 2012; Hayasaki et al., 2013).

Our study focuses on meanders of several hundred kilometers in size due to the highly idealized nature of the SST fields considered. In reality, WBCs exhibit much finer and more complex structures, including mesoscale eddies and submesoscale fronts, which must be considered to accurately represent atmospheric circulation in weather and climate models (Foussard et al., 2019; Czaja et al., 2019; Seo et al., 2023). Notably, Vivant et al. (2025) show that ocean submesoscale fronts can locally induce diabatic heating within storms. Such interactions—along with atmosphere–ocean coupling—are not represented in our framework, which constitutes a major limitation. Nevertheless, our results demonstrate that storms respond to diabatic forcing from SST anomalies within just a few hours.

Open Research Section

The code and model data needed to reproduce the figures in this manuscript will be deposited in a publicly accessible GitHub repository and assigned to a DOI prior to publication.

Acknowledgments

This work is a contribution to the joint projects I-CASCADE and POSEIDON funded by the French CNES TOSCA program. This work was granted access to the HPC resources of IDRIS under the allocation AD010106852R2 made by GENCI (Grand Equipement National de Calcul Intensif).

Author contributions

F.V.: Conceptualization, Data curation, Formal analysis, Investigation, Methodology, Software, Validation, Visualization, Writing – original draft

G.L.: Conceptualization, Funding acquisition, Investigation, Methodology, Software, Validation, Writing – original draft

References

Booth, J. F., Thompson, L., Patoux, J., & Kelly, K. A. (2012). Sensitivity of midlatitude storm intensification to perturbations in the sea surface temperature near the gulf stream. *Monthly Weather Review*, *140*(4), 1241–1256.

Brayshaw, D. J., Hoskins, B., & Blackburn, M. (2008). The storm-track response to idealized sst perturbations in an aquaplanet gcm. *Journal of the Atmospheric Sciences*, *65*(9), 2842–2860.

Browning, K. (1997). The dry intrusion perspective of extra-tropical cyclone development. *Meteorological Applications*, *4*(4), 317–324.

Bui, H., & Spengler, T. (2021). On the influence of sea surface temperature distributions on the development of extratropical cyclones. *Journal of the Atmospheric Sciences*, *78*(4), 1173–1188.

Chen, S.-H., & Sun, W.-Y. (2002). A one-dimensional time dependent cloud model. *Journal of the Meteorological Society of Japan. Ser. II*, *80*(1), 99–118.

Czaja, A., Frankignoul, C., Minobe, S., & Vannière, B. (2019). Simulating the midlatitude atmospheric circulation: what might we gain from high-resolution modeling of air-sea interactions? *Current climate change reports*, *5*(4), 390–406.

Dacre, H. F., Martinez-Alvarado, O., & Mbengue, C. O. (2019). Linking atmospheric rivers and warm conveyor belt airflows. *Journal of Hydrometeorology*, *20*(6), 1183–1196.

de Vries, H., Scher, S., Haarsma, R., Drijfhout, S., & Delden, A. v. (2019). How gulf-stream sst-fronts influence atlantic winter storms: Results from a downscaling experiment with harmonie to the role of modified latent heat fluxes and low-level baroclinicity. *Climate Dynamics*, *52*(9), 5899–5909.

Demirdjian, R., Doyle, J. D., Finocchio, P. M., & Reynolds, C. A. (2022). On the influence of surface latent heat fluxes on idealized extratropical cyclones. *Journal of the Atmospheric Sciences*, *79*(9), 2229–2242.

Deremble, B., Lapeyre, G., & Ghil, M. (2012). Atmospheric dynamics triggered by an oceanic sst front in a moist quasigeostrophic model. *Journal of the Atmospheric Sciences*, *69*(5), 1617–1632.

Foussard, A., Lapeyre, G., & Plougonven, R. (2019). Storm track response to oceanic eddies in idealized atmospheric simulations. *Journal of Climate*, *32*(2), 445–463.

Hayasaki, M., Kawamura, R., Mori, M., & Watanabe, M. (2013). Response of extratropical cyclone activity to the kuroshio large meander in northern winter. *Geophysical Research Letters*, *40*(11), 2851–2855.

Hirata, H., Kawamura, R., Kato, M., & Shinoda, T. (2015). Influential role of moisture supply from the kuroshio/kuroshio extension in the rapid development of an extratropical cyclone. *Monthly Weather Review*, *143*(10), 4126–4144.

Jiménez, P. A., Dudhia, J., González-Rouco, J. F., Navarro, J., Montávez, J. P., & García-Bustamante, E. (2012). A revised scheme for the wrf surface layer formulation. *Monthly weather review*, *140*(3), 898–918.

Joyce, T. M., Kwon, Y.-O., & Yu, L. (2009). On the relationship between synoptic wintertime atmospheric variability and path shifts in the gulf stream and the kuroshio extension. *Journal of Climate*, *22*(12), 3177–3192.

Kain, J. S. (2004). The kain–fritsch convective parameterization: an update. *Journal of applied meteorology*, *43*(1), 170–181.

Kelly, K. A., Small, R. J., Samelson, R., Qiu, B., Joyce, T. M., Kwon, Y.-O., & Cronin, M. F. (2010). Western boundary currents and frontal air–sea interaction: Gulf stream and kuroshio extension. *Journal of Climate*, *23*(21), 5644–5667.

Larson, J. G., Thompson, D. W., & Hurrell, J. W. (2024). Signature of the western boundary currents in local climate variability. *Nature*, *634*(8035), 862–867.

Lorenz, E. N. (1955). Available potential energy and the maintenance of the general circulation. *Tellus*, *7*(2), 157–167.

Ma, X., Chang, P., Saravanan, R., Montuoro, R., Nakamura, H., Wu, D., ... Wu, L. (2017). Importance of resolving kuroshio front and eddy influence in simulating the north pacific storm track. *Journal of Climate*, *30*(5), 1861–1880.

Mellor, G. L., & Yamada, T. (1982). Development of a turbulence closure model for geophysical fluid problems. *Reviews of Geophysics*, *20*(4), 851–875.

Minobe, S., Kuwano-Yoshida, A., Komori, N., Xie, S.-P., & Small, R. J. (2008). Influence of the gulf stream on the troposphere. *Nature*, *452*(7184), 206–209.

Moore, R. W., & Montgomery, M. T. (2005). Analysis of an idealized, three-dimensional diabatic rossby vortex: A coherent structure of the moist baroclinic atmosphere. *Journal of the atmospheric sciences*, *62*(8), 2703–2725.

Nakamura, H., Nishina, A., & Minobe, S. (2012). Response of storm tracks to bimodal kuroshio path states south of japan. *Journal of Climate*, *25*(21), 7772–7779.

Nakamura, H., Sampe, T., Tanimoto, Y., & Shimpo, A. (2004). Observed associations among storm tracks, jet streams and midlatitude oceanic fronts. *Earth's Climate: The Ocean–Atmosphere Interaction, Geophys. Monogr*, *147*, 329–345.

O'Reilly, C. H., & Czaja, A. (2015). The response of the pacific storm track and

atmospheric circulation to kuroshio extension variability. *Quarterly Journal of the Royal Meteorological Society*, *141*(686), 52–66.

Orlanski, I., & Sheldon, J. P. (1995). Stages in the energetics of baroclinic systems. *Tellus A*, *47*(5), 605–628.

Parfitt, R., Czaja, A., Minobe, S., & Kuwano-Yoshida, A. (2016). The atmospheric frontal response to sst perturbations in the gulf stream region. *Geophysical Research Letters*, *43*(5), 2299–2306.

Qiu, B., Chen, S., Schneider, N., & Taguchi, B. (2014). A coupled decadal prediction of the dynamic state of the kuroshio extension system. *Journal of Climate*, *27*(4), 1751–1764.

Seo, H., O'Neill, L. W., Bourassa, M. A., Czaja, A., Drushka, K., Edson, J. B., ... others (2023). Ocean mesoscale and frontal-scale ocean–atmosphere interactions and influence on large-scale climate: A review. *Journal of climate*, *36*(7), 1981–2013.

Shaw, T., Baldwin, M., Barnes, E. A., Caballero, R., Garfinkel, C., Hwang, Y.-T., ... others (2016). Storm track processes and the opposing influences of climate change. *Nature Geoscience*, *9*(9), 656–664.

Sheldon, L., Czaja, A., Vannière, B., Morcrette, C., Sohet, B., Casado, M., & Smith, D. (2017). A 'warm path'for gulf stream–troposphere interactions. *Tellus A: Dynamic Meteorology and Oceanography*, *69*(1), 1299397.

Skamarock, W. C., Klemp, J. B., Dudhia, J., Gill, D. O., Liu, Z., Berner, J., ... others (2019). A description of the advanced research wrf model version 4. *National Center for Atmospheric Research: Boulder, CO, USA*, *145*(145), 550.

Vannière, B., Czaja, A., Dacre, H., & Woollings, T. (2017). A "cold path" for the gulf stream–troposphere connection. *Journal of Climate*, *30*(4), 1363–1379.

Vivant, F., Siegelman, L., Klein, P., Torres, H. S., Menemenlis, D., & Molod, A. M. (2025). Ocean submesoscale fronts induce diabatic heating and convective precipitation within storms. *Communications Earth & Environment*, *6*(1), 69.

Zhang, X., Ma, X., & Wu, L. (2019). Effect of mesoscale oceanic eddies on extratropical cyclogenesis: A tracking approach. *Journal of Geophysical Research: Atmospheres*, *124*(12), 6411–6422.

Supporting Information for "Meandering ocean currents modulate mid-latitude storm energetics"

Félix Vivant[1]and Guillaume Lapeyre[1]

[1]LMD-IPSL, ENS, PSL Université, Ecole Polytechnique, IP Paris, Sorbonne Université, CNRS, Paris, France

Contents of this file

1. Text S1 to S3
2. Table S1
3. Figures S1 to S2

Introduction

This document describes the model configuration and the prescribed initial conditions for the ocean and the atmosphere.

Text S1: Precision on the WRF configuration and conventions

Simulations use a time step of 100 s, with model outputs stored hourly. A vertical-velocity damping layer, 5 km deep below the model top, is applied to reduce gravity wave reflection (Klemp et al., 2008). In the following, we define the coordinate system such that x, y, and z denote the zonal, meridional, and vertical axes, respectively. The experiment domain spans 16000 km in the x-direction and 6000 km in the y-direction. By convention, the origin $(x, y) = (0, 0)$ is set at the location of the initial cyclonic

perturbation, which is centered meridionally and located 2000 km east of the western boundary of the domain. In this reference frame, the simulation domain is defined as: $(x, y) \in [-2000 \text{ km}, 14000 \text{ km}] \times [-3000 \text{ km}, 3000 \text{ km}]$. Unless stated otherwise, $z = 0$ corresponds to the surface. In Equations 4–9, however, we use the convention $z = 0$ at the reference tropopause height (Z_{trop}).

Text S2: Sea surface temperature fields

In all experiments, the atmospheric model is forced by a sea surface temperature (SST) field of the following form:

$$\text{SST}(x, y) = \text{SST}_{\text{eq}} - \frac{\Delta\text{SST}}{2}\left[1 + \tanh\left(2\frac{g_{\text{SST}}}{\Delta\text{SST}}(y - y^*(x))\right)\right] \tag{1}$$

where $\text{SST}_{\text{eq}} = 21°\text{C}$ is the temperature at the southern boundary, and $\Delta\text{SST} = 15°\text{C}$ is the SST difference between the northern and the southern boundaries. $g_{\text{sst}} = 3°\text{C (100km)}^{-1}$ is the maximum SST gradient in absolute value. The SST function of $y - y^*(x)$ is shown in Figure S1a. The function $y^*(x)$ defines the shape of the SST front, which varies across experiments:

$$y^*_{\text{CTL}}(x) = 0 \quad \forall\, x \tag{2}$$

$$y^*_{\text{M}}(x) = \begin{cases} \frac{l_{\text{SST}}}{2} \sin\left(\pi \frac{x - x_{\text{SST}}}{l_{\text{SST}}}\right) & \text{for } x \in [x_{\text{SST}}, x_{\text{SST}} + \Delta x_{\text{SST}}] \\ 0 & \text{else} \end{cases} \tag{3}$$

where $y^*_{\text{CTL}}(x)$ is a zonal SST front, and $y^*_{\text{M}}(x)$ represents a meandering SST front (Figure S1b). The typical meanders size, l_{SST}, is 500 km in M5 and 1000 km in M10 (Fig-

ure S1b). In both M5 and M10, the meanders begin at $x_{\mathrm{SST}} = 1000$ km, and extend zonally over 4000 km.

Text S3: Initial atmospheric state

The initial atmospheric state is adapted from Bui and Spengler (2021) and consists of a zonally symmetric jet and a cyclonic perturbation, as presented in Figure S2. The jet is defined by a wind field $\overline{u}(y, z)$ (Equations 4-9), a vertical potential temperature profile $\overline{\theta}(y_{\mathrm{ref}}, z)$ (Equation 10), and a reference pressure $\overline{p}(y_{\mathrm{ref}}, 0) = p_0$ (Table S1). The reference latitude is set to $y_{\mathrm{ref}} = -3000$ km, corresponding to the southern boundary. All constants and their descriptions are provided in Table S1. As mentioned above, the jet is defined by the following set of equations:

$$\overline{u}(y, z) = U_0 \, W_y(y) \, W_z(z^*) \tag{4}$$

$$W_y(y) = \begin{cases} \cos^2\left(\frac{\pi}{2} \frac{y - y_{\mathrm{jet}}}{L_y}\right) & \text{for } |y - y_{\mathrm{jet}}| \leq L_y \\ 0 & \text{else} \end{cases} \tag{5}$$

$$z^*(y, z) = z - A \tanh\left(\frac{5}{2} \frac{y_{\mathrm{jet}} - y}{L_y}\right) \tag{6}$$

$$A(z) = \begin{cases} 0 & \text{for } z < -L_z \\ |z_{\mathrm{jet}} - z_{\mathrm{trop}}| \sin\left(\frac{\pi}{2} \frac{L_z + z}{L_z}\right) & \text{for } -L_z \leq z \leq 0 \\ |z_{\mathrm{jet}} - z_{\mathrm{trop}}| & \text{for } z > 0 \end{cases} \tag{7}$$

$$W_z(z) = \begin{cases} 1 + C(\frac{z}{l_1})^2[\frac{1}{6}(\frac{z}{l_1})^2 - 1] & \text{for } |z| \le l_1 \\ w_0 - \alpha|z| & \text{for } l_1 < |z| < L_z - l_2 \\ \frac{\alpha l_2}{2}(\frac{L_z - |z|}{l_2})^3(2 - \frac{L_z - |z|}{l_2}) & \text{for } L_2 - l_2 \le |z| \le L_z \\ 0 & \text{for } |z| > L_z \end{cases} \tag{8}$$

with

$$l_1 = l_2 = 0.04\, L_z,\ w_0 = \frac{1}{1 - \frac{3}{8}\frac{l_1}{L_z - 0.5\, l_2}},\ C = \frac{3}{4}\alpha l_1 \text{ and } \alpha = \frac{w_0}{L_z - 0.5\, l_2} \tag{9}$$

$\overline{\theta}$ is defined as follows:

$$\theta(y = y_{\text{ref}}, z) = \begin{cases} \theta_0 \exp\left(\frac{N^2_{\text{trop}}\, z}{g}\right) & \text{for } z \le z_{\text{trop}} \\ \theta(y_{\text{ref}}, z_{\text{trop}}) \exp\left(\frac{N^2_{\text{stra}}(z - z_{\text{trop}})}{g}\right) & \text{for } z > z_{\text{trop}} \end{cases} \tag{10}$$

The cyclonic perturbation is defined as an axisymmetric pressure anomaly centered at (x_p, y_p):

$$p'(x, y, z) = \begin{cases} \Delta p \cos^2(\frac{\pi}{2}\frac{z}{H_p})(1 - R^2)^3 & \text{for } R < 1 \text{ and } z < H_p \\ 0 & \text{else} \end{cases} \tag{11}$$

where $R = \sqrt{(x - x_p)^2 + (y - y_p)^2}/R_p$. Applying the hydrostatic balance yields the density anomaly:

$$\rho'(x, y, z) = \begin{cases} \frac{\pi \Delta p}{2 g H_p} \sin(\pi \frac{z}{H_p})(1 - R^2)^3 & \text{for } R < 1 \text{ and } z < H_p \\ 0 & \text{else} \end{cases} \tag{12}$$

The moisture content is initialized using a vertical profile of relative humidity:

$$\mathrm{rh}(z) = \mathrm{rh}_0 \exp\Big[-0.5\Big(\frac{z}{z_{\mathrm{rh}}}\Big)^4\Big] \tag{13}$$

The full initial state—that is, the zonal jet plus the perturbation—is determined using geostrophic and hydrostatic balances coupled with the ideal gas law. We proceed as follows:

• First, we perform a numerical integration using a 4th-order Runge-Kutta scheme (RK4) to impose hydrostatic balance, coupled with the ideal gas law. Starting from a reference potential temperature profile $\overline{\theta}(y_{\mathrm{ref}}, z)$ and a surface pressure $\overline{p}(y_{\mathrm{ref}}, 0) = p_0$, we compute the reference pressure profile $\overline{p}(y_{\mathrm{ref}}, z)$ for all z. The corresponding reference density $\overline{\rho}(y_{\mathrm{ref}}, z)$ is then obtained via the equation of state.

• Second, we apply successive RK4 integrations of the geostrophic and hydrostatic balances to determine the full jet fields: $\overline{p}(y, z)$, $\overline{\theta}(y, z)$, and $\overline{\rho}(y, z)$. At iteration i, the pressure field $\overline{p}_i(y, z)$ is computed from $\overline{\theta}_{i-1}(y, z)$ and the zonal wind $\overline{u}$ via the geostrophic balance. For the first iteration, we initialize $\overline{\theta}_0(y, z) = \overline{\theta}(y_{\mathrm{ref}}, z)$ for all y. The density field $\overline{\rho}_i(y, z)$ is then computed from $\overline{p}_i(y, z)$ via the hydrostatic balance, and the updated potential temperature field $\overline{\theta}_i(y, z)$ is derived using the ideal gas law. We perform 10 iterations to ensure convergence.

• Finally, we construct the full fields by adding perturbations: $p = \overline{p} + p'$ and $\rho = \overline{\rho} + \rho'$. The temperature is obtained from the ideal gas law, and the full wind field (u, v) is diagnosed using geostrophic balance. The water vapor mixing ratio is calculated from the

relative humidity profile and taken into account in the equation of state via the virtual temperature.

References

Bui, H., & Spengler, T. (2021). On the influence of sea surface temperature distributions on the development of extratropical cyclones. *Journal of the Atmospheric Sciences*, *78*(4), 1173–1188.

Klemp, J., Dudhia, J., & Hassiotis, A. (2008). An upper gravity-wave absorbing layer for nwp applications. *Monthly Weather Review*, *136*(10), 3987–4004.

Table S1. Physical parameters of the initial atmospheric state

Name	Value	Description
f	$1,028 \times 10^{-4}$ s^{-1}	Coriolis parameter of the f-plane at 45°N
U_0	50 m.s^{-1}	Jet maximum wind speed
z_{jet}	8 km	Altitude of the jet core
L_y	1000 km	Meridional extend of the jet
L_z	10 km	Vertical extend of the jet
p_0	1008 hPa	Sea level pressure at the southern boundary
θ_0	295 K	Surface potential temperature at the southern boundary
z_{trop}	10 km	Tropopause height at the southern boundary
N^2_{trop}	10^{-4} s^{-2}	Static stability in the troposphere
N^2_{stra}	5.6×10^{-4} s^{-2}	Static stability in the stratosphere
rh_0	0.5	Relative humidity at the surface
z_{rh}	8 km	Vertical extent of the relative humidity profile
R_p	500 km	Radius of the initial perturbation
H_p	6 km	Vertical extent of the initial perturbation
Δp	2 hPa	Magnitude of the initial perturbation
x_p	0 km	Initial location of the perturbation along the x-axis
y_p	0 km	Initial location of the perturbation along the y-axis

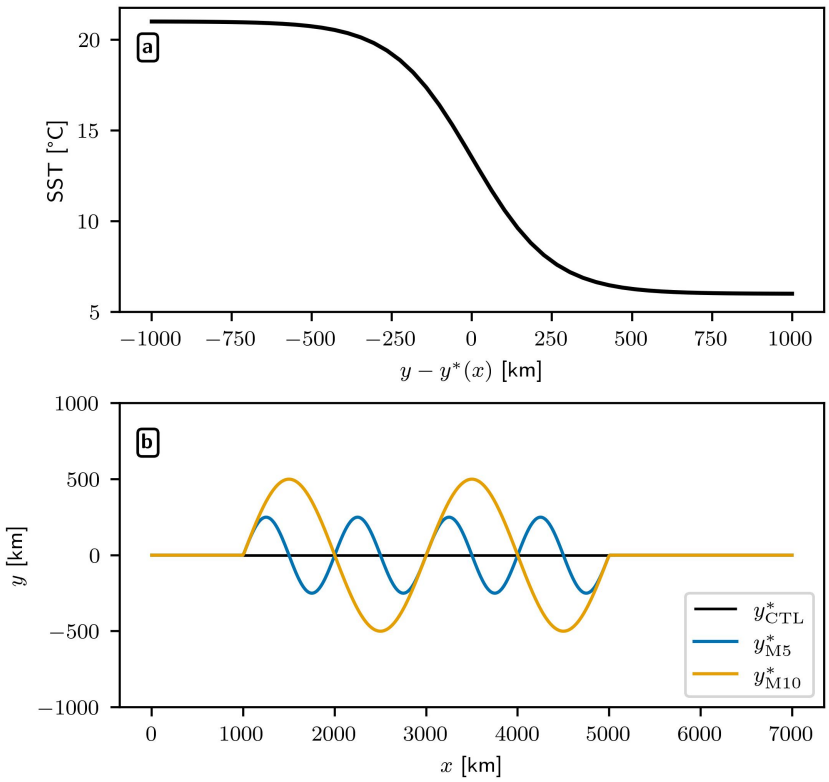

Figure S1. Idealized sea surface temperature fronts. (a) SST profile as a function of $y - y^*(x)$ (Equation 1). (b) Shape of the SST fronts ($y^*(x)$, Equations 2 and 3) for CTL (black), M5 (blue) and M10 (orange).

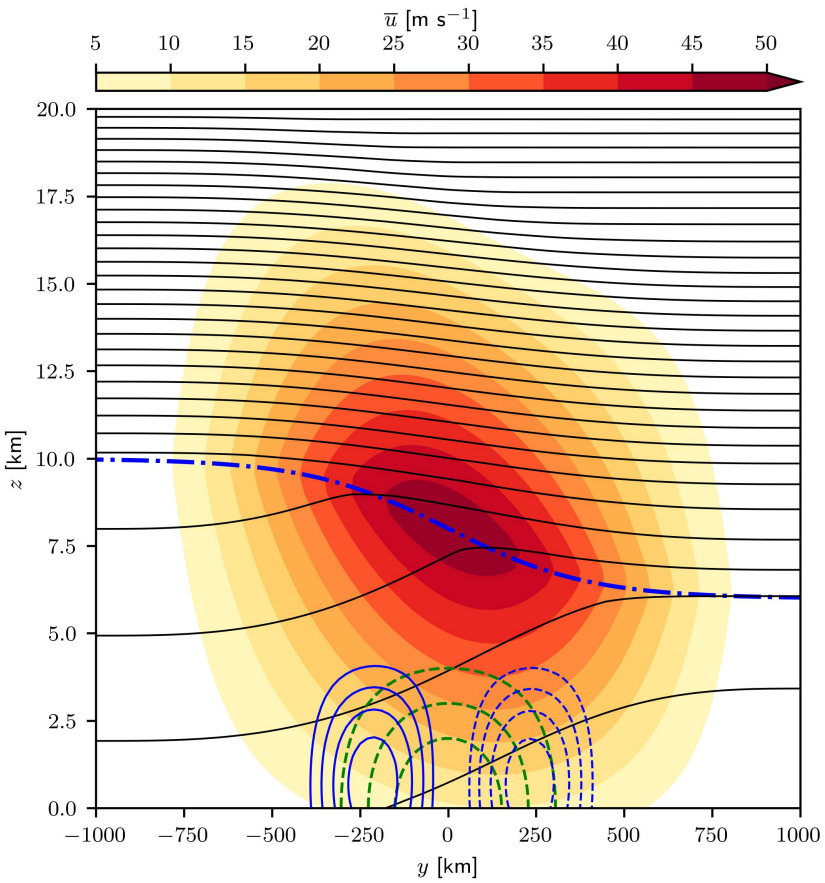

Figure S2. Idealized atmospheric state. Jet stream zonal wind ($\overline{u}$, shading) and potential temperature ($\overline{\theta}$, black contours from 300 K to 570 K every 10 K). Tropopause height (dash-dotted blue line), pressure perturbation ($p'(x_p, y)$, green contours at -1.5, -1, and -0.5 hPa) and associated zonal wind perturbation ($u - \overline{u}$, blue contours from -5 to -2 m s^{-1} and from 2 to 5 m s^{-1}). Dashed contours indicate negative values.